Egypt. J. Chem. **Vol. 68**, No. 12 pp. 489 - 501 (2025)

Egyptian Journal of Chemistry

http://ejchem.journals.ekb.eg/

Investigating the Effect of Zn_2SnO_4Nanoparticles on Structural, Optical, and Electrical Properties of PVA Nanocomposites

M.M.Saadeldin[a,]*, Ahmed Samir[a], Fawzy G. El Desouky[b]

[a]*Physics Department, Faculty of Science, Cairo University, Giza 12613, Egypt*
[b]*Solid State Physics Department, Physics Research Division, National Research Centre, Cairo, 12622, Egypt*

Abstract

This study reports the fabrication and comprehensive characterization of novel polymer composite films comprised of hydrothermally synthesized zinc tin oxide nanoparticles (ZTO-NP) embedded within a polyvinyl alcohol (PVA) matrix. The systematic investigation focuses on elucidating the effects of varying ZTO-NP concentrations (5%, 8%, and 10%) on the structural, morphological, optical, and electrical properties of the resulting nanocomposites. X-ray Diffraction (XRD) confirms the successful synthesis of crystalline cubic-phase ZTO-NP, which act as nucleating agents to enhance crystallinity in the PVA matrix. Fourier Transform Infrared (FTIR) spectroscopy validates interfacial interactions between nanoparticles and polymer chains. Scanning Electron Microscopy (SEM) and Atomic Force Microscopy (AFM) demonstrate concentration-dependent surface roughness due to nanoparticle aggregation and dispersion. Diffuse Reflectance Spectroscopy (DRS) reveals improved UV absorption with increasing ZTO-NP loading, with optimal performance observed at 8% concentration due to balanced dispersion and minimized optical band gap. Electrical characterization highlights tunable dielectric relaxation behavior and increased AC conductivity, attributed to space charge defect generation. These findings underscore the potential of ZTO/PVA nanocomposites for advanced applications in optoelectronics, UV shielding, and next-generation electronic devices, offering a versatile route to engineering multifunctional materials.

Keywords: Nanocomposites; Thin-film; XRD; SEM; AFM; Optical properties; Dielectric properties.

Introduction

Polymer-based nanocomposites have emerged as a prominent area of research due to their ability to combine the inherent characteristics of polymers with the enhanced properties of nanoparticle fillers. These advanced materials exhibit exceptional optical, mechanical, electrical, and chemical properties, making them suitable for a broad range of applications, including optoelectronics, sensors, and micro-optics [1, 2]. Amongst the various polymers used in nanocomposites, polyvinyl alcohol (PVA) stands out as a versatile and biodegradable material with excellent film-forming capability, strong dielectric properties, high mechanical strength, and water solubility. PVA's unique molecular structure, characterized by hydroxyl groups along its backbone, facilitates hydrogen bonding and allows for the stabilization of nanoparticles, preventing aggregation and ensuring homogeneous nanocomposite formation [2, 3]. Films of PVA also have UV-shielding capabilities, giving them excellent anti-UV properties [1].

Zinc oxide (ZnO) and tin dioxide (SnO_2) are well-known n-type semiconductors widely used in optoelectronics, gas sensing, and photocatalysis. However, their practical applications are often constrained by limitations such as high operating temperatures, low sensitivity, and poor selectivity. To address these challenges, heterostructure engineering has emerged as a promising approach that leverages the synergistic effects of combining multiple metal oxides [4]. Zinc tin oxide (Zn2SnO4 or ZTO) is a material that integrates the advantageous properties of ZnO and SnO2, offering high electron mobility, excellent electrical conductivity, and superior optical characteristics. These features make ZTO particularly attractive for applications in solar cells, photocatalysis for environmental remediation, gas sensors, and optoelectronic devices such as transparent conducting oxides and UV light absorbers [5, 6]. The use of PVA as a host matrix for ZTO nanoparticles provides additional advantages due to its ability to act as a capping agent and stabilize nanoparticles chemically and environmentally. The dielectric properties of PVA, combined with its optical transparency and strong interactions with nanoparticles through hydrogen bonding, make it an ideal candidate for applications requiring optical clarity and high charge storage capacity [7]. Furthermore, parameters such as nanoparticle size, shape, concentration, and dispersion within the polymer matrix

*Corresponding author e-mail: mmmounir@sci.cu.edu.eg.; (M.M.Saadeldin).
Received date 11 March 2025; Revised date 04 April 2025; Accepted date 11 May 2025
DOI: 10.21608/ejchem.2025.367456.11437

significantly influence the structural, optical, and electrical performance of nanocomposites. Careful optimization of these factors is critical to achieving superior multifunctional properties [8, 9].

Prior research has explored PVA/ZTO nanocomposites for various applications. For instance, studies have demonstrated the effectiveness of ZTO in enhancing the UV-shielding properties of PVA films. However, a significant limitation in these studies is the tendency of ZTO nanoparticles to aggregate within the PVA matrix, leading to non-uniform dispersion and compromised optical and electrical properties. Moreover, many existing methods for synthesizing ZTO nanoparticles require high temperatures and complex procedures, which can be energy-intensive and costly.

This study addresses these limitations through a novel approach involving the hydrothermal synthesis of ZTO nanoparticles followed by their integration into a PVA matrix. The hydrothermal method allows for the synthesis of highly crystalline ZTO nanoparticles at relatively low temperatures, ensuring better control over particle size and morphology. Furthermore, this study systematically investigates the effects of varying ZTO-NP concentrations (5%, 8%, and 10%) on the structural, morphological, optical, and electrical properties of the resulting nanocomposites, providing a comprehensive understanding of the structure-property relationships. By optimizing the ZTO concentration and employing a controlled hydrothermal synthesis, this research aims to improve the dispersion of ZTO-NP within the PVA matrix, enhance the optical and electrical properties of the nanocomposite, and offer a more efficient and cost-effective method for producing high-performance PVA/ZTO nanocomposites.

Experimental

3.1. Materials and Synthesis of ZTO-NP via Hydrothermal Method

Zinc acetate dihydrate (Sigma-Aldrich, 99.99% trace metals basis) and tin chloride dihydrate (Sigma-Aldrich, 99.99%) were separately prepared as 0.1 mol solutions in 30 ml of distilled water. Subsequently, these solutions were mixed in varying molar ratios to achieve the desired composition of ZTO-NP. The mixed metal salt solutions were then added drop-wise to a stirred solution of distilled water at room temperature. The reaction mixture was then placed inside a 100 ml sealed hydrothermal reactor and heated for 24 hours at 180°C. After the hydrothermal reaction, the reactor was allowed to cool to room temperature, and centrifugation was used to gather the precipitated ZTO-NP (5000 RPM for 15 minutes). The resulting nanoparticles (NP) were washed multiple times with distilled water and ethanol to remove any remaining reactants or byproducts. Finally, the washed NP was dried at a moderate temperature (60°C under a vacuum) for two days and annealed at 700° C in air for five hours to obtain ZTO powder.

3.2. Preparation of ZTO/PVA Composite at Different Concentrations

Polyvinyl alcohol (PVA, Mw = 89,000-98,000 g/mol, 341584 Sigma-Aldrich) powder was dissolved in distilled water at 80°C under stirring to prepare a 10 wt % PVA solution. The number of ZTO-NP needed for each loading percentage S1 (5% ZTO /PVA), S2 (8% ZTO /PVA), and S3 (10% ZTO /PVA) was calculated based on the total weight of the PVA solution. The calculated amount of ZTO-NP was then mixed into the PVA solution under sonication to ensure uniform dispersion. Subsequently, the ZTO /PVA solution was cast into a petri dish and allowed to dry at 60°C (relative humidity of 50%) for two days.

3.3. Measurement Techniques

The structural properties of ZTO-NP and ZTO/PVA samples were analyzed using an X-ray diffractometer (RigakuUltima III) with CuKα radiation (λ = 1.5406 Å) over the 2θ range of 20°–80°. Fourier transform infrared (ATR-FTIR) spectra were recorded using a Bruker Vertex 80 spectrometer to identify functional groups and chemical bonding in the samples. Optical properties were evaluated through diffuse reflectance spectra of the samples measured at room temperature using a Jasco High-Performance UV/VIS/NIR spectrophotometer (model V-770, Japan) in the spectral range of 190–1000 nm. The surface morphology and elemental composition of the samples were examined using scanning electron microscopy (SEM) FEI Model FEI Inspect S50 after sputter-coating with gold. Additionally, atomic force microscopy (AFM; model Wet-SPM9600, Shimadzu, Japan) in non-contact mode (using a silicon tip with a resonant frequency of 300 kHz and a spring constant of 40 N/m) was used to study the nanoscale surface features and dispersion of nanoparticles. Dielectric properties and AC conductivity were measured using a high-resolution Novocontrol Alpha Analyzer, employing a parallel plate capacitor configuration. Broadband dielectric spectroscopy provided detailed insights into the electrical behavior of the composites under varying conditions (frequency range: 1 Hz to 5 MHz).

4. Results and discussion

4.1. X-ray Diffraction

X-ray diffraction (XRD) analysis was employed to identify the composition and crystalline phases in the samples. The diffraction patterns of ZTO-NP, PVA, and ZTO/PVA samples with varying ZTO-NP concentrations were analyzed using Bragg's law for peak indexing [10]. **Figure 1A** compares the XRD patterns of ZTO synthesized via the hydrothermal method with those of pure ZnO and SnO_2. The ZTO-NP pattern exhibits characteristic diffraction peaks at 17.72°, 29.12°, 34.29°, 35.91°, 41.66°, 45.40°, 51.67°, 55.02°, and 60.39°, corresponding to the (111), (220), (311), (222), (400), (331), (422), (511), and (440) planes, respectively. These peaks match the standard JCPDS card (74-2184) for ZTO, confirming its crystalline cubic phase (space group $Fd\bar{3}m$, 227) with a preferred orientation in the (311) plane. The ZnO phase shows peaks at 31.68°, 36.23°, 47.53°, 56.57°, 62.85°, 67.94°, and 69.06°, corresponding to planes (100), (101), (102), (110), (103), (112), and (201), consistent with JCPDS card (89-1397). The hexagonal structure of ZnO (space group P63mc, 186) has a preferred orientation in the (101) plane. For SnO_2, peaks at 26.52°, 37.90°, 57.81°, 61.78°, and 65.74° correspond to planes (110), (200), (002), (310), and (301), matching the JCPDS card (88-0287) for the tetragonal rutile phase (space group P42/mnm, 136) with a preferred orientation in the (110) plane [11]. The absence of extraneous peaks confirms the purity of the synthesized ZTO-NP and the successful integration of the SnO**2**, ZnO, and ZTO phases. These findings validate the effectiveness of the synthesis method, with results aligning with prior studies [12].

Figure 1B shows the XRD patterns of pure PVA and ZTO/PVA samples at different concentrations (S**1**, S**2**, and S**3**). The intensity of diffraction peaks increases with increasing concentration of ZTO-NP, indicating enhanced crystallinity in the

samples. The crystallinity, relative to pure PVA, is increased by factors of 1.38 for sample **S1**, 4.02 for sample **S2**, and 4.79 for sample **S3**. This increase in crystallinity may be attributed to the role of ZTO-NP as nucleating agents. When ZTO-NP are dispersed within the PVA matrix, these nanoparticles act as sites for the nucleation of crystalline regions, promoting a higher degree of order. Furthermore, good compatibility between ZTO-NP and PVA enhances interfacial interactions, facilitating the ordered packing of PVA chains around the nanoparticles [13]. This improved chain alignment contributes to the overall increase in crystallinity observed in the samples. These results confirm the high crystalline quality of ZTO and ZTO/PVA samples, where ZTO concentrations play a crucial role in determining the crystallinity and structural properties of the samples [14].

The crystallite size (D**s**) was calculated from XRD data using the Debye-Scherrer equation [15]:

$$D_s = \frac{k\lambda}{\beta \cos\theta} \quad \text{---------- (1)}$$

Where λ is the wavelength of the copper radiation source (1.54056 Å) of the X-Ray device, k is a dimensionless shape factor typically 0.9, β_{hkl} is the full-width at half maximum (FWHM) of the diffraction peak in radians after correcting for instrumental broadening $\beta_{hkl} = \left[\beta^2_{Observed} - \beta^2_{instrument}\right]^{1/2}$, and θ is the Bragg angle (diffracting peak position).

The instrumental broadening was considered and calibrated using standard Si samples. The Debye-Scherrer equation was applied to calculate the crystallite size from the highest peak along the (110), (100), and (311) planes for SnO2, ZnO, and ZTO, respectively.

Dislocation density (δ) was calculated using the following equation [16-18]:

$$\delta = \frac{1}{D_s^2} \quad \text{---------- (2)}$$

Where D**s** is the crystallite size.

The calculated crystallite sizes and dislocation densities for all samples are presented in **Table 1**. The diffraction patterns indicate that the increase in ZTO concentration leads to a more crystalline structure compared to pure-phase materials, as predicted by the Scherrer formula. The calculated δ values decrease with increasing ZTO concentration.

Table 1: Structural parameters of crystallite size (D_s) and dislocation density (δ) for ZTO powder, pure PVA, S_1, S_2, and S_3.

Sample	Phase	D_s (nm)	δ(nm^{-2})
ZTO	ZTO	28.57	12.25
	ZnO	43.56	5.27
	SnO_2	13.73	53.05
S_1	PVA	5.13	379.98
	ZTO	34.77	8.27
	ZnO	47.7	4.39
	SnO_2	18.38	29.60
S_2	PVA	4.98	403.21
	ZTO	37.45	7.13
	ZnO	18.68	28.65
	SnO_2	20.75	23.22
S_3	PVA	5.16	375.57
	ZTO	36.36	7.56
	ZnO	62.55	2.56
	SnO_2	8.28	145.86

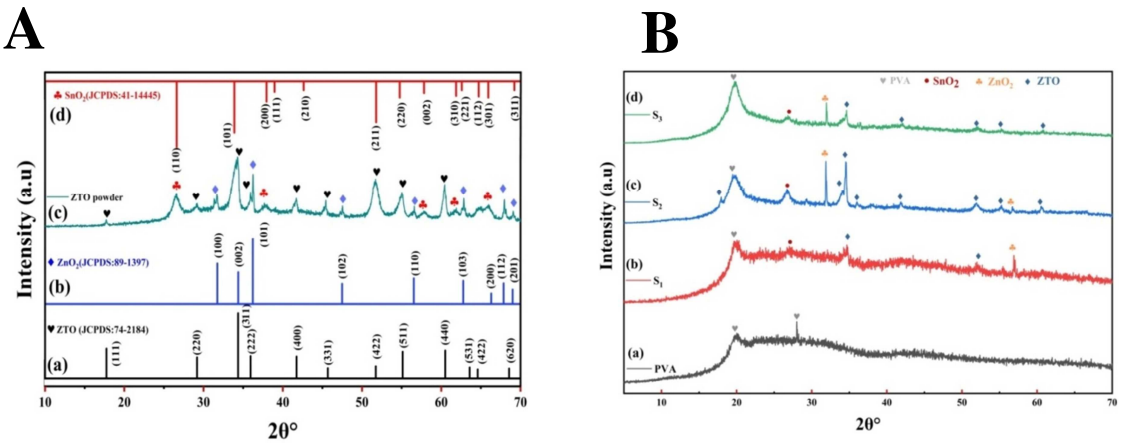

Figure1: X-ray diffraction patterns of: (A) ZTO-NP, ZnO, and SnO_2 compared to JCPDS standards, and (B) pure PVA and ZTO/PVA composites (S_1, S_2, and S_3).

4.2 Fourier transforms infrared spectroscopy (FTIR)

The FTIR analysis provides insights into the chemical bonding and interactions in the ZTO-NP and ZTO/PVA samples. **Figure 2A** shows the FTIR spectrum of ZTO-NP. Key peaks are observed at approximately 690 cm^{-1}, 530 cm^{-1}, and 425 cm^{-1},

which can be attributed to the stretching vibrations of Sn-O, Sn-O-Zn, and Zn-O bonds, respectively, the peak around 414 cm^{-1} corresponding to the Zn-O-Zn bond [18, 19]. These peaks confirm the successful formation of the ZTO phase. **Figure 2B** shows the FTIR spectra of pure PVA and the ZTO/PVA composites (S_1, S_2, and S_3). In the spectrum of pure PVA (**Figure 2a**), characteristic peaks are observed at: 3267 cm^{-1} (O-H stretching vibration, intermolecular hydrogen bonding), 2942 cm^{-1} , and 2906 cm^{-1} (C-H stretching vibration), 1726 cm^{-1} (C=O stretching, residual acetate groups), 1422 cm^{-1} (C-H bending), 1088 cm^{-1} (C-O stretching), and 917 cm^{-1} (C-C stretching) [20, 21].

Upon incorporation of ZTO-NP into the PVA matrix, several changes are observed in the FTIR spectra of the composites (**Figures 2b-d**). The intensity of the broad O-H stretching band at ~3267 cm^{-1}decreases with increasing ZTO concentration, suggesting a reduction in intermolecular hydrogen bonding within the PVA matrix due to interactions with the ZTO nanoparticles [22]. This could be due to the formation of hydrogen bonds between the hydroxyl groups of PVA and the oxygen atoms on the surface of the ZTO nanoparticles. Additionally, the shift in the ZTO related bands can indicate the changes in the vibrational modes [23]. As the ZTO loading increases, the peak at 425 cm^{-1} and 690 cm^{-1} shows the band shift. These shifts suggest the presence of interactions and confirm the blending of the PVA matrix and the ZTO nanoparticles which confirm successful incorporation of ZTO-NP into the PVA matrix [24].

The FTIR results, combined with the XRD analysis, provide evidence of the successful integration of ZTO-NP within the PVA matrix and the chemical interactions between the components.

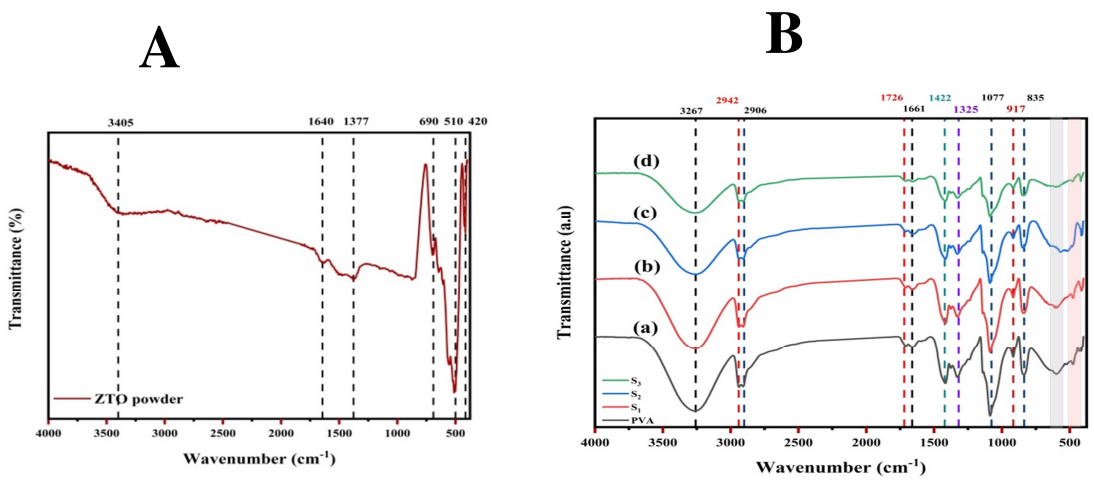

Figure 2: FTIR spectra of (A) ZTO nanoparticles (ZTO-NP) and (B) pure PVA and ZTO/PVA nanocomposites (S_1, S_2, and S_3) in the wavenumber range of 400–4000 cm^{-1}, where a) pure PVA, b) S_1 c) S_2, and d) S_3.

4.3 Surface morphology

4.3.1 Scanning Electron Microscope (SEM) morphology

SEM was employed to investigate the influence of ZTO-NP incorporation on the surface morphology of PVA. **Figure 3** presents representative SEM images of pure PVA and ZTO/PVA nanocomposites (S_1, S_2, and S_3). **Figure 3a** reveals that the surface of pure PVA is relatively smooth and featureless, indicative of its pristine nature. Upon the addition of ZTO-NP in S_1 (**Figure 3b**), the surface exhibits a noticeable increase in irregularities. The ZTO-NP are dispersed across the PVA matrix, displaying a generally uniform distribution, although some degree of nanoparticle aggregation is observed [25]. Preliminary particle size analysis (using Image J software) indicated an average ZTO-NP aggregate size of approximately 50-75 nm in this sample. Increasing the ZTO-NP concentration in S_2 (**Figure 3c**) results in the formation of larger clusters compared to S_1. The average aggregate size increases to approximately 100-150 nm, indicating a reduction in the uniformity of nanoparticle dispersion [26].

At a ZTO-NP concentration in S_3 (**Figure 3d**), the surface morphology is characterized by pronounced nanoparticle aggregation and a highly uneven texture. Large agglomerates of ZTO-NP are evident, with average aggregate sizes exceeding 200 nm. This indicates a significant departure from uniform dispersion and suggests that the surface energy of the ZTO-NP dominates over their interaction with the PVA matrix at these high loadings [26, 27].

The observed aggregation behavior can be attributed to several factors. Firstly, the high surface energy of the ZTO-NP promotes their self-assembly into larger aggregates to minimize their surface area. Secondly, at higher concentrations, the nanoparticles may exceed the saturation limit for stable dispersion within the PVA matrix, leading to increased aggregation [28]. Finally, PVA chain entanglement may also play a role, as the polymer chains may not be able to effectively encapsulate and stabilize the nanoparticles at high ZTO-NP loadings. The SEM images demonstrate a clear correlation between increasing ZTO-NP concentration and alterations in surface morphology. Specifically, higher ZTO-NP loadings lead to increased surface roughness and greater nanoparticle aggregation. These morphological changes are expected to influence the optical and electrical properties of the ZTO/PVA nanocomposites, emphasizing their importance in tailoring material properties for specific applications.

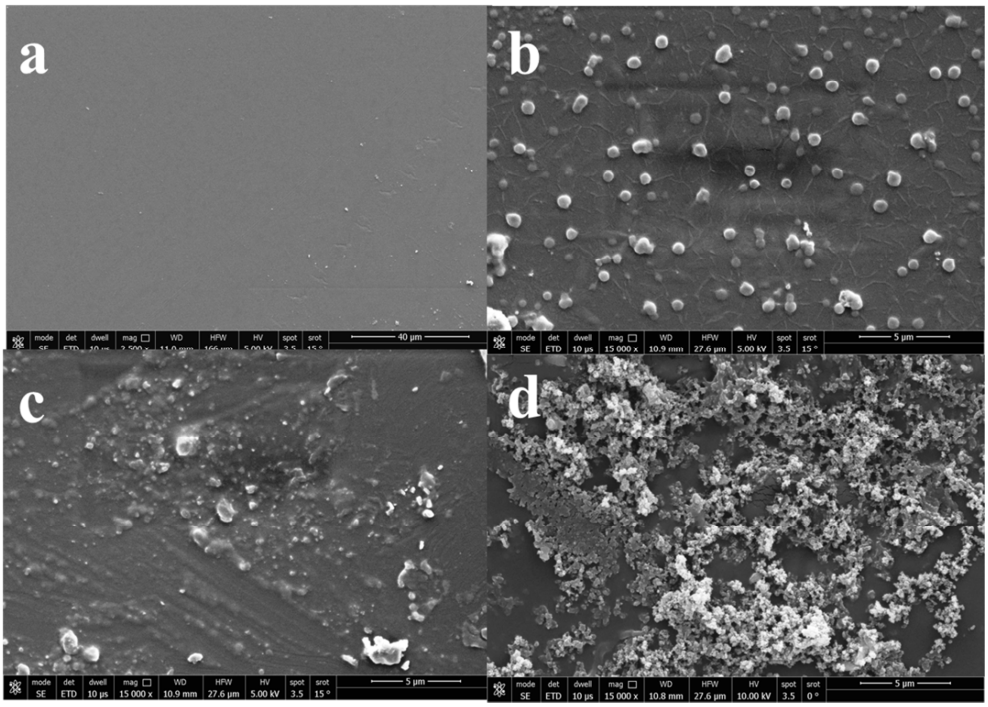

Figure 3: SEM images of (a) pure PVA, (b) S_1, (c) S_2, and (d) S_3 with fixed magnification 15000x for S_1, S_2, and S_3.

4.3.2 Atomic Force Microscopy (AFM) Morphology

The surface morphology and roughness of ZTO/PVA nanocomposites were analyzed using AFM. **Figure 4** illustrates representative 2D and 3D AFM topographic images at (5 µm × 5 µm scan size) of pure PVA and ZTO/PVA samples S_2 and S_3. Key roughness parameters, including arithmetic mean roughness (R_a) and root-mean-square roughness (R_q), were extracted from the AFM data to characterize the surface texture quantitatively (**Table 2**). The AFM image of pure PVA (**Figure 4a**) depicts a relatively smooth surface with minimal irregularities, indicative of low surface roughness. The measured R_a and R_q values for pure PVA were 4.51 nm and 5.98 nm, respectively. Upon incorporation of ZTO-NP, a significant alteration in surface roughness was observed. The R_a and R_q values for samples S_2 and S_3 are substantially higher than those of pure PVA, as detailed in **Table 2** [29].

The observed increase in surface roughness with increasing ZTO-NP concentration in the PVA matrix can be attributed to nanoparticle aggregation, non-uniform dispersion, and potential phase separation within the composite. The higher ZTO-NP loading leads to the formation of larger agglomerates, resulting in a more irregular and corrugated surface topography. These surface modifications are expected to influence the optical, mechanical, adhesive, and electrical properties of the material, which are critical to its intended applications. A fundamental understanding of the correlation between surface roughness and nanoparticle concentration is, therefore, essential for tailoring the composite material to achieve optimal performance for specific applications [29, 30].

Theoretical considerations suggest that for a Gaussian distribution of asperity heights, the ratio of R_q to R_a should approximate 1.25. Empirical observations by Ward indicate that this ratio may reach up to 1.31 in engineering surfaces. The (R_q/ R_a) value obtained from AFM analysis for sample S_3 (1.26) is consistent with the theoretical prediction of 1.25, while the value for sample S_2 (1.34) is more closely aligned with Ward's empirical observation. This alignment suggests that the asperity height distribution reasonably follows a Gaussian model at the scale of AFM imaging. Also, the increased roughness observed in S_2 and S_3 can impact surface interactions, potentially affecting adhesion and friction properties [31, 32].

Table 2: Roughness parameters of pure PVA and ZTO/PVA samples (S_2 and S_3), where R_a(arithmetic mean roughness), R_z (maximum height), R_{zjis} (10-point mean roughness), R_q(root-mean-square roughness), R_p (average height), and R_v (average depth).

Region	R_a(nm)	R_q(nm)	R_z(nm)	R_{zjis}(nm)	R_p(nm)	R_v(nm)	R_q/R_a
Pure PVA	4.51	5.98	65.99	31.86	45.20	20.79	1.33
S_2	20.45	27.31	222.14	106.66	142.92	79.23	1.34
S_3	41.14	51.87	544.26	240.93	222.52	318.75	1.26

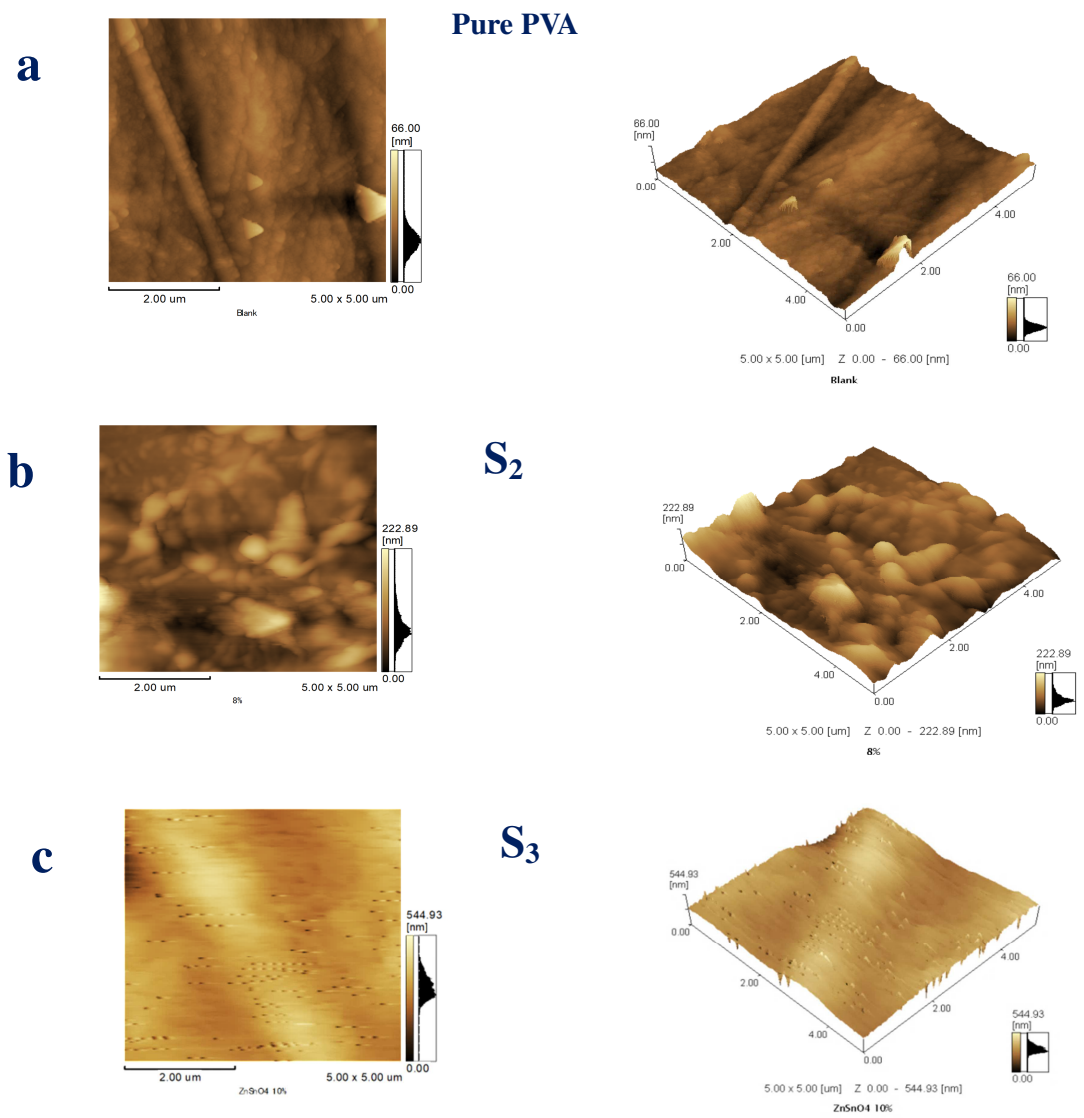

Figure 4: AFM 2D and 3D topographic images of: (a) Pure PVA, (b) S_2, and (c) S_3.

4.4 Optical properties

The optical properties of samples were investigated to determine their optical bandgap (E_g)**.Figure 5a** illustrates the absorption spectra of pure PVA and the ZTO/PVA nanocomposite samples (S_1, S_2, and S_3). Pure PVA exhibits minimal UV absorbance; however, the incorporation of ZTO-NP significantly enhances UV absorption [33]. This enhancement suggests increased crystallinity within the composite, a finding supported by XRD data [34]. As the concentration of ZTO-NP increases, a shift in the optical absorption edge toward higher wavelengths is observed. This shift is attributed to charge transfer transitions within the material [35]. Furthermore, the change in color from transparent (pure PVA) to semi-transparent in the nanocomposites confirms broader light absorption, positioning these materials as potential UV absorbers. Notably, sample S_2 demonstrates superior absorption compared to S_3, which can be attributed to the aggregation of ZTO-NP at higher concentrations, leading to a less effective distribution of the nanoparticles. **Figure 5b** displays the absorption coefficient (α) as a function of photon energy (hν), calculated using equation 3 [36]:

$$\alpha = \frac{2.302}{d} \log \frac{I_0}{I} \qquad \text{---------- (3)}$$

Where d represents the sample thickness, and I_0 and I denote the intensities of the incident and transmitted light, respectively. The optical bandgapE_g was then evaluated using Tauc's formula (equation 4) [37]:

$$\alpha\, h\nu = \beta(h\nu - E_g)^{\gamma} \qquad \text{---------- (4)}$$

Where hν is the incident photon energy, β is a constant, E_g is the optical bandgap, and **γ** is an exponent that depends on the nature of the electronic transition. Specifically, γ values of 1/2, 2, 3/2, or 3 correspond to allowed direct, allowed indirect, forbidden direct, and forbidden indirect transitions, respectively. The bandgap values were determined by analyzing two spectral ranges: 210–240 nm (range 1) and 290–340 nm (range 2). Tauc plots of αhν versus hν were utilized to extract the bandgap values. The quality of the fits was assessed using the R-squared (R^2) values [38, 39].

The samples exhibit direct allowed transitions. This behavior is attributed to the complex electronic band structure of the material, which allows for various types of transitions, including direct transitions at specific points within the Brillouin zone. These direct allowed transitions occur when the electronic states involved meet the symmetry requirements dictated by selection rules. This dual nature of transitions in Zn_2SnO_4 significantly contributes to its unique optical properties, making it a material of significant interest for a range of applications [33].

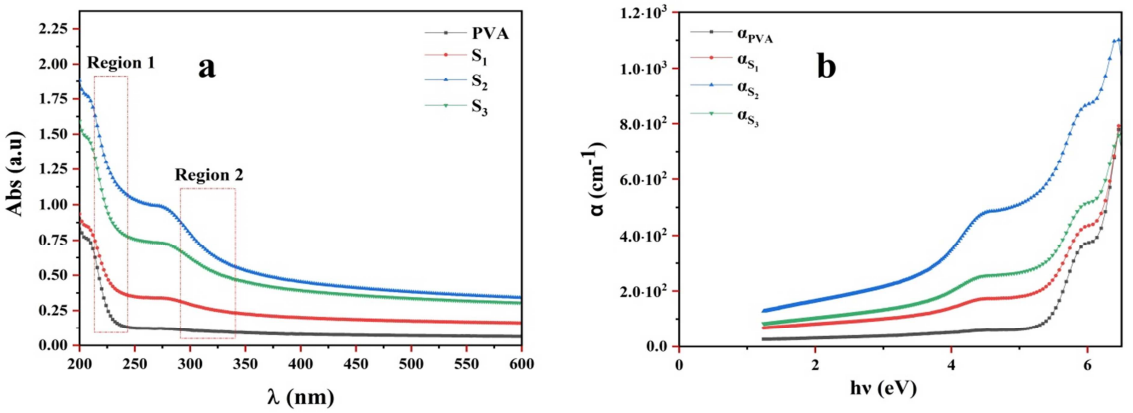

Figure 5: UV–Vis (DRS) analysis including (a) absorbance as a function of wavelength and (b) absorption coefficient (α) as a function of photon energy (hν) for pure PVA and nanocomposite samples S_1, S_2, and S_3.

Figure 6a presents the optical bandgap of ZTO-NP for directly allowed transitions. The inset of **Figure 6a** reveals three strong absorption bands, corresponding to three distinct phases, at 3.21 eV, 3.39 eV, and 3.49 eV. These bands are attributed to the presence of ZnO, SnO_2 and ZTO phases, respectively. **Figure 6a** also shows that pure PVA exhibits a single strong absorption band at approximately 5.55 eV. Upon doping with ZTO-NP, the samples display two strong absorption bands. The first absorption region appears at 5.37 eV, 5.20 eV, and 5.16 eV, while the second absorption region is observed at 3.50 eV, 3.74 eV, and 3.80 eV; all these transitions are classified as direct allowed transitions. The combination of ZTO and PVA lead to a reduction in the bandgap, as summarized in **Table 3**, which details the change in bandgap for direct allowed transitions in samples with varying ZTO-NP concentrations. **Figures 6b, c**, and **d** illustrate the optical energy bandgap of ZTO/PVA samples decreasing with increasing ZTO-NP concentration compared to pure PVA, as summarized in **Table 3**. This trend is attributed to the ability of the ZTO-NP to organize within the PVA matrix, leading to modifications in the energy levels and a consequent reduction in the bandgap [40, 41].

.

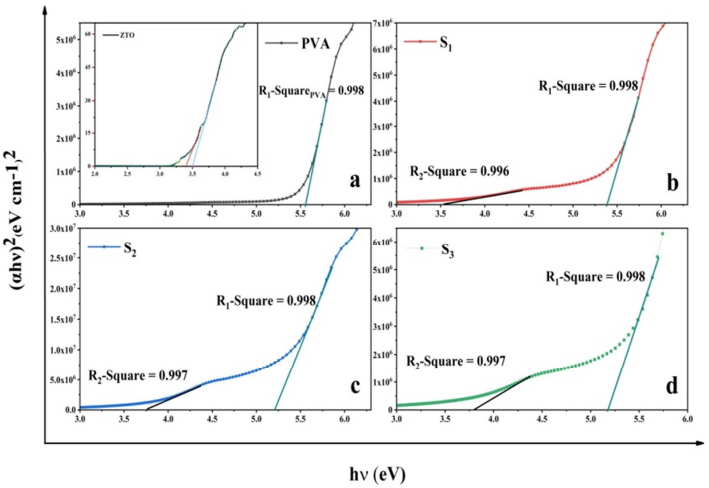

Figure 6: Optical bandgap for direct allowed transitions for (a) Pure PVA (inset: ZTO-NP), (b) S_1, (c) S_2, and (d) S_3.

Table 3: Optical bandgap values for direct allowed transitions in pure PVA and ZTO/PVA samples (S_1, S_2, and S_3).

Sample	Bandgap 1 (eV)	Bandgap 2 (eV)
PVA	5.55	------
ZTO-NP	------	3.49
S_1	5.37	3.52
S_2	5.20	3.74
S_3	5.16	3.80

4.5 Dielectric properties

The dielectric properties of PVA and ZTO/PVA nanocomposites (S_1, S_2, and S_3) were investigated as a function of frequency at room temperature. **Figures 7a**, and **b** show the frequency dependence of the real part (ε') and imaginary part (ε") of the complex permittivity (ε*) for the samples. The real part ε' represents the material's ability to store electrical energy, while ε" represents the energy dissipation within the material. As depicted in **Figure 7**, both ε' and ε" decrease with increasing frequency for all samples. This behavior is consistent with the Maxwell-Wagner-Sillars (MWS) polarization mechanism, which is typical in heterogeneous materials. The MWS effect arises from the accumulation of charge carriers at the interfaces between the ZTO nanoparticles (NP) and the PVA matrix, creating interfacial polarization.

At lower frequencies, interfacial polarization dominates the dielectric response. Charge carriers accumulate at the interfaces between the ZTO-NP and the PVA matrix, leading to a high capacitance and a large value of ε'. Notably, the nanocomposites exhibit higher ε' values compared to pure PVA, particularly at lower frequencies. Specifically, sample S_3 shows the highest ε' values in this region (**Figure 7a**). This suggests that the introduction of ZTO-NP enhances the material's ability to store electrical energy [42, 43].

However, as the frequency increases, the charge carriers are unable to keep pace with the alternating electric field. This results in a reduction of interfacial polarization, leading to a decrease in both ε' and ε". Furthermore, the rate of decrease in both ε' and ε" appears to be influenced by the ZTO concentration. Observe that the S_1 sample shows the lowest values for both parameters (**Figures 7 a, b**). This may be indicative of differences in charge carrier mobility and interfacial interactions within the nanocomposites. In essence, the real and imaginary parts of dielectric permittivity depend on ZTO concentration [44-46].

The real part of the dielectric permittivity (ε') was calculated using the following equation [42]:

$$\varepsilon' = \frac{Cd}{A\varepsilon_0} \qquad \text{---------- (5)}$$

Where: C is the capacitance (F), d is the thickness of the sample (m), A is the area of the electrode (m^2), and ε_0 is the permittivity of free space (8.85×10^{-12} F/m).

The dielectric loss factor (Tan δ) was calculated from the real and imaginary parts of the complex permittivity:

$$\text{Tan } \delta = \frac{\varepsilon''}{\varepsilon'} \qquad \text{---------- (6)}$$

Where: ε" is the imaginary part of the permittivity, and ε' is the real part of the permittivity.

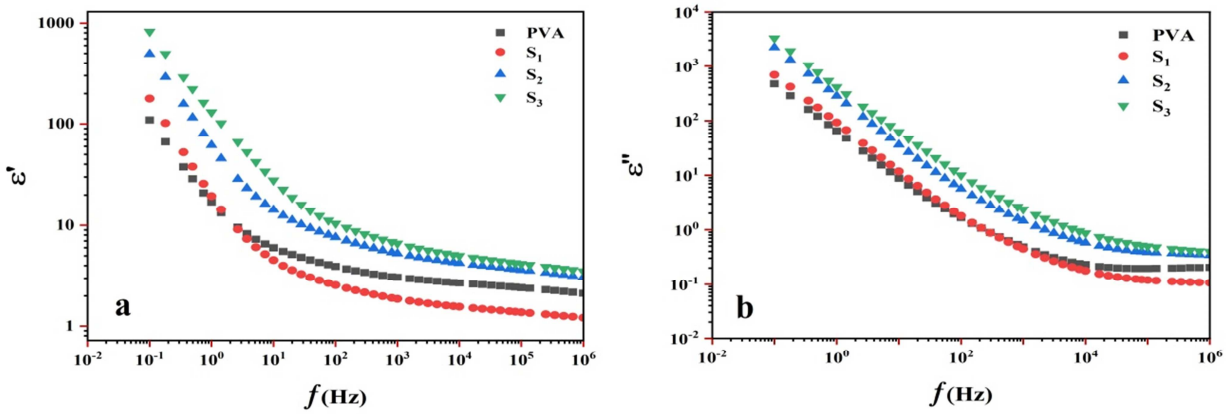

Figure 7: Frequency dependence for the dielectric permittivity (a) real part ε′, and (b) imaginary part ε″ for pure PVA and ZTO/PVA samples.

To further analyze the dielectric behavior, the Havriliak-Negami (H-N) model was applied to the real permittivity (dielectric constant) of the pure PVA and ZTO/PVA nanocomposites with different concentrations at room temperature. The H-N model is particularly useful for representing the relaxation behavior of materials that exhibit non-Debye relaxation [47, 48]. The complex permittivity (ε*(ω)) according to the H-N model, and the real and imaginary parts of the H-N equation are given by:

$$\varepsilon = \varepsilon_\infty + \frac{\Delta\varepsilon}{(1+(i\omega\tau)\beta)^\gamma} \qquad \text{---------- (7)}$$

$$\varepsilon' = \varepsilon_{\infty} + \Delta\,\varepsilon^{*}(w) * ((w)) \quad \text{---------- (8)}$$

$$(w) = \left[1 + 2(w\tau_{HN})^{\beta}\cos\left(\frac{\beta\pi}{2}\right)(w\tau_{HN})^{2\beta}\right]^{-\gamma/2} \quad \text{---------- (9)}$$

$$(w) = \arctan\left[\frac{\sin\left(\frac{\beta\pi}{2}\right)}{(w\tau_{HN})^{-\beta} + \cos\left(\frac{\beta\pi}{2}\right)}\right] \quad \text{---------- (10)}$$

$$\varepsilon'' = \Delta\,\varepsilon^{*}(w) * \sin(\gamma\varphi(w)) + \frac{\sigma'}{w^{s}} \quad \text{---------- (11)}$$

Where: ε∞ represents the permittivity at the high-frequency limit, ε_s is the static permittivity at low frequency, $\Delta\varepsilon = \varepsilon_s - \varepsilon_\infty$ denotes the dielectric strength. w is the angular frequency, τ_{HN} is the characteristic relaxation time associated with the H-N model,γ and β are shape parameters with values between 0 and 1, describing the symmetric and asymmetric broadening of the dielectric spectrum. The fit function builder in Origin Lab Pro (version 21) was utilized to achieve the best fit for the experimental data using the H-N equation, allowing for the extraction of key parameters from the fitting process (see **Table 4**). **Figure 8** displays the H-N model fitting for the samples, demonstrating a strong correspondence between the experimental measurements and the theoretical predictions.

Table 4 presents the key values used in the fitting process of the H-N equation for pure PVA and ZTO/PVA samples. The increase in Δε with higher concentrations of ZTO nanoparticles in the PVA matrix suggests enhanced interfacial polarization, increased particle loading, and the contribution of polarizable ZTO nanoparticles. These factors collectively improve the dielectric response of the composite, leading to higher dielectric strength.

Table 4: Shows the values of the Havriliak-Negami (H-N) fitting parameters for pure PVA and ZTO/PVA samples.

Sample	$\Delta\varepsilon$	β	γ	τ	ε_{inf}
PVA	222	1	0.7	17	3.1
S_1	357.7285	1	0.77732	13.70935	1.57321
S_2	965.2572	1	0.75	13.87615	4.3362
S_3	1565.631	1	0.68972	15	4.78888

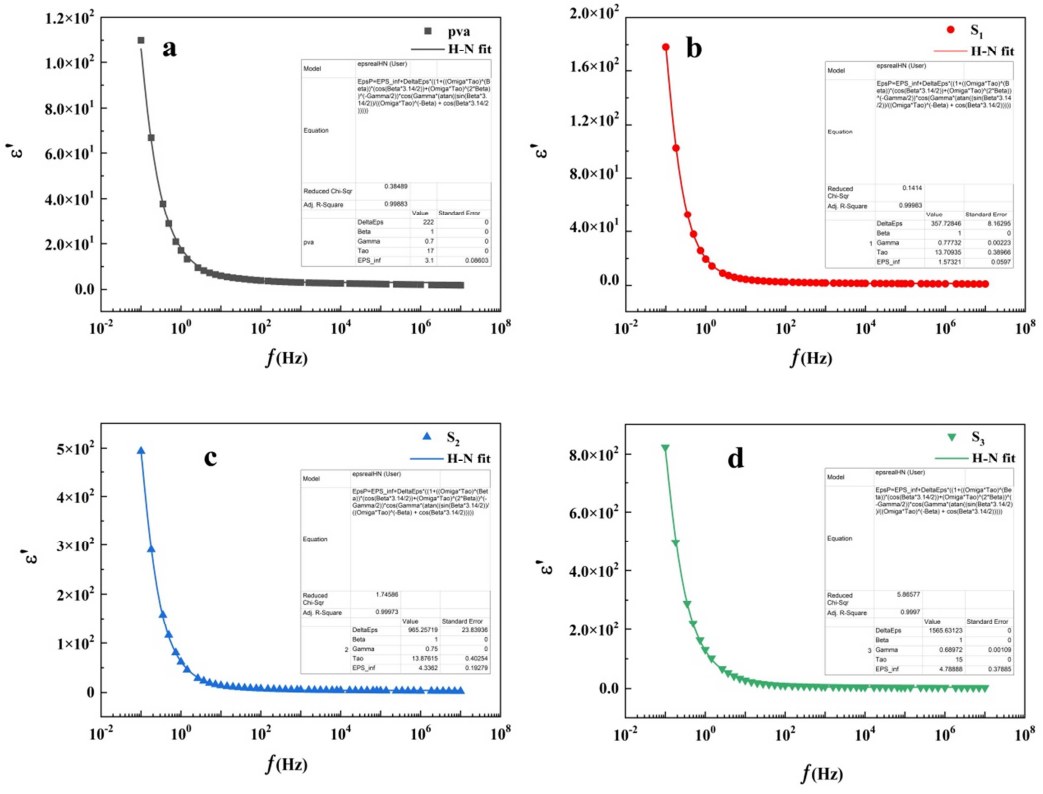

Figure 8: Havriliak-Negami (H-N) model fitting data for (a) pure PVA, (b) S_1, (c) S_2, and (d) S_3.

The loss tangent (Tan δ) (or the dielectric loss), measured the energy dissipated within the material due to polarization processes. **Figure 9a** shows the frequency dependence of Tan δ for the PVA and ZTO/PVA nanocomposites (S_1, S_2, and S_3). As frequency increases, the dielectric loss generally decreases. This is related to the time lag between the applied electric field and the polarization response of the material. Specifically, at lower frequencies (below 10^2 Hz), the addition of ZTO NP leads to an increase in Tan δ compared to pure PVA, while at higher frequencies, the values converge. The AC conductivity (σ) represents the ability of the material to conduct alternating current. **Figure 9b** shows the frequency dependence of σ for the samples (S_1, S_2, and S_3) [49]. AC conductivity was determined using the equation:

$$\sigma = 2\pi f \varepsilon_0 \varepsilon'' \quad \text{---------- (11)}$$

Where: f is the frequency (Hz), ε_0 is the permittivity of free space (8.85 × 10-12 F/m), and ε" is the imaginary part of the permittivity.

The introduction of ZTO-NP generally increases the AC conductivity of the PVA matrix. This can be attributed to the generation of space charge defects by the ZTO-NP, which enhances charge carrier mobility [50]. As seen in **Figure 9b**, S_2 and S_3 exhibit significantly higher conductivity than PVA and S_1 across the measured frequency range. However, the conductivity of S_1 is even less than pure PVA. This suggests that low ZTO concentration reduces AC conductivity. At low frequencies, the conductivity may be lower due to the trapping of charge carriers at the interfaces. However, at higher frequencies, these trapped charges can be detrapped, leading to a significant increase in conductivity. This behavior can be explained by Koop's phenomenological model, which attributes the dielectric behavior of heterogeneous materials to the presence of grain boundaries or interfaces. The ZTO-NP also facilitates interactions between polymer chains, potentially reducing cohesive tension and enhancing chain segmental motion [51, 52].

It's important to note that while increasing ZTO NP concentration generally enhances conductivity up to a certain point, very high concentrations may lead to a decrease in certain dielectric characteristics (specifically, the decrease in ε" at higher frequencies, as seen in **Figure 7b**) due to constrained ionic mobility within the matrix [53]. Additionally, although S_2 and S_3 exhibit higher AC conductivity, Tan δ decreases with ZTO NP concentration. This suggests that these concentrations of ZTO NP contribute more to the loss of energy.

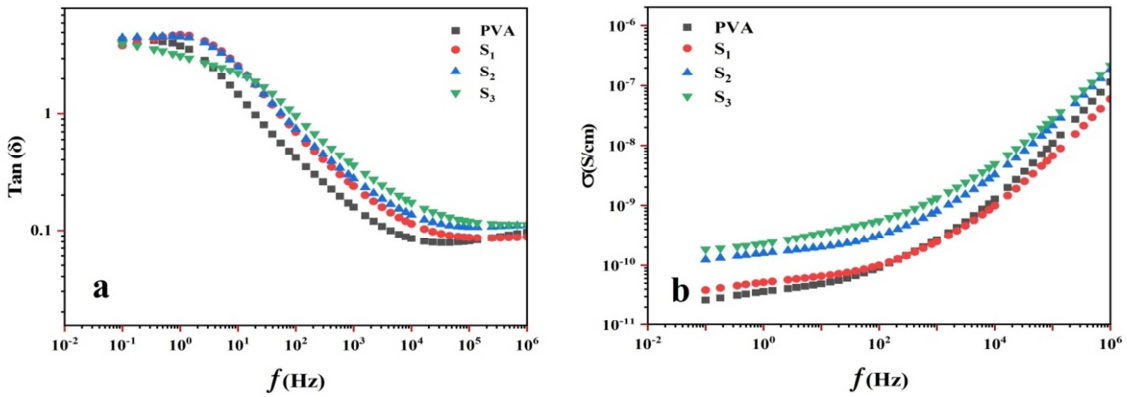

Figure 9: a) Variation of tangent loss Tan δ, and b) Variation of AC conductivity, as a function of frequency (f)

The electric modulus formalism is used to analyze the relaxation behavior of the materials, minimizing the effects of electrode polarization. The real (M') and imaginary (M") parts of the electric modulus are shown in **Figure 10**.

Figure 10a shows the M' as a function of frequency. At low frequencies, the M' tends to increase due to the accumulation of charge carriers or polarization effects within the material. As shown in **Figure 10a**, at all frequencies, S_1 shows the largest M', PVA and S_2 intermediate and S_3 the lowest M' values. As the frequency increases, more charge carriers contribute to the overall response, leading to an increase in M'. Additionally, as the frequency continues to increase, the material may reach a point where its response becomes saturated beyond 10^3 Hz. This saturation occurs when all available charge carriers are fully mobilized, and further increases in frequency do not significantly affect the polarization dynamics. Therefore, M' stabilizes or plateaus at higher frequencies [54].

Figure 10b illustrates the M" as a function of frequency. At lower frequencies, M" increases with frequency, similar to M'. This increase is attributed to the accumulation of charge carriers or the reorientation of dipoles in response to the applied electric field. As the frequency increases, more charge carriers can respond to the field, leading to enhanced polarization and, consequently, an increase in M" [55]. However, unlike M', M" reaches a maximum value at a certain frequency (around 10^2 Hz) and then decreases. S_1 exhibits the biggest M" peak value, and S_3 the smallest. At frequencies beyond this maximum, the response of the material is constrained by factors such as relaxation time or interfacial polarization, resulting in a slower rate of polarization change and a decrease in M". At very high frequencies, the material may exhibit more or less inert behavior, where polarization effects are minimal, causing M" to decrease. Eventually, M" stabilizes or reaches a plateau at a value close to zero, indicating that the material's response to the electric field has fully saturated, and additional frequency increases do not induce further polarization [56].

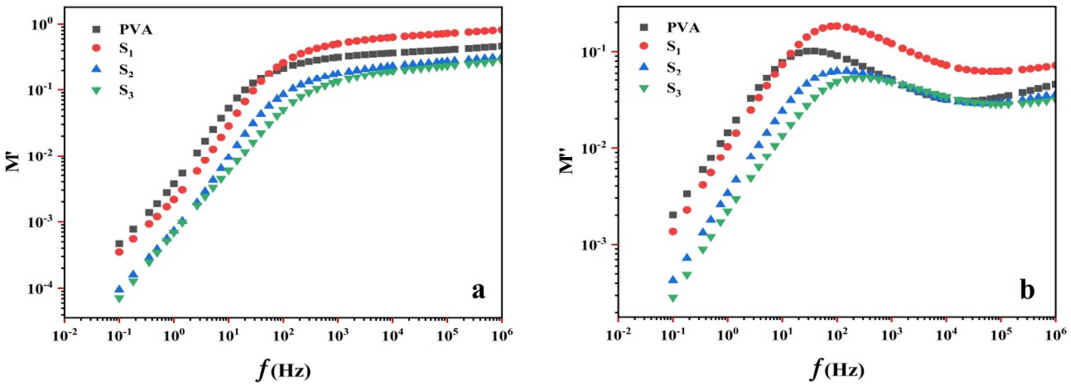

Figure 10: Electric modulus as a function of frequency (f) of a) the real electric modulus M′, and b) the imaginary electric modulus M″

Figure 11 illustrates the complex modulus (M′ vs. M″) plots for PVA and ZTO/PVA nanocomposites (S_1, S_2, and S_3). The semicircular shape observed is characteristic of relaxation processes, such as dielectric relaxation. The size of the semi-circle is related to the relaxation strength. As shown in **Figure 11**, sample S_1 shows a larger semicircle than PVA, indicating that, at low ZTO concentrations, the increased mobility of charge carriers results in a larger semi-circle, meaning enhanced relaxation. Conversely, samples S_2 and S_3 show smaller semicircles, meaning that, at higher concentrations, interactions between the ZTO nanoparticles hinder charge carrier mobility, leading to a smaller semicircle, which indicates suppressed relaxation. The addition of ZTO significantly influences dielectric relaxation: at lower concentrations, it enhances the relaxation process, enlarging the semi-circle (S_1), while at higher concentrations, it suppresses relaxation, resulting in a reduced semi-circle (S_2, S_3). Interfacial effects also contribute to this behavior. At low ZTO concentrations, interfacial interactions promote relaxation, whereas at higher concentrations, these interfaces become less effective [57, 58].

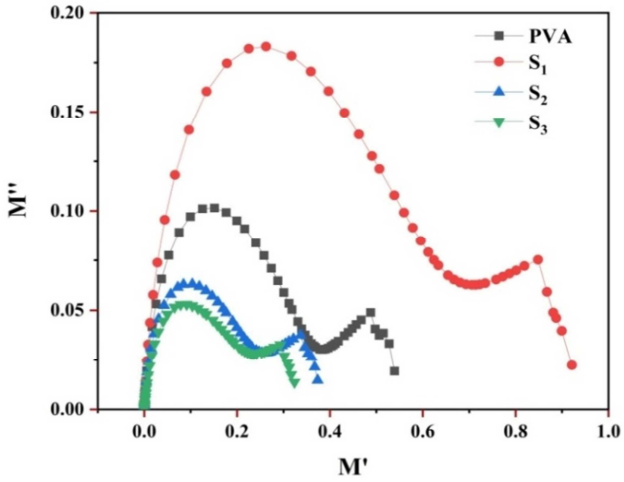

Figure 11: M' vs. M" for pure PVA and ZTO/PVA samples (S_1, S_2, and S_3).

Conclusions

The successful synthesis and integration of ZTO nanoparticles into a PVA matrix have demonstrated significant improvements in structural, optical, and electrical properties, making these nanocomposites highly promising for practical applications. The enhanced crystallinity achieved through the nucleating effect of ZTO-NP, coupled with improved UV absorption and tunable electrical conductivity, positions these materials as ideal candidates for optoelectronic devices, high-performance UV shielding films, and flexible electronics. Notably, the optimal performance observed at 8% ZTO concentration provides a critical benchmark for achieving balanced nanoparticle dispersion and superior material properties. This study highlights the applied significance of ZTO/PVA nanocomposites in addressing challenges related to material engineering for advanced technologies. Future research can further explore their potential in specific applications such as solar cells, transparent conductors, and environmental remediation systems.

Credit authorship contribution statement

M.M. Saadeldin: conceptualization, review, resources, validation, editing, visualization, supervision. Ahmed Samir: conceptualization, methodology, formal analysis, validation, writing, original draft, visualization, editing. Fawzy G. El Desouky: review, supervision, conceptualization, resources.

Acknowledgments
This work is supported by Cairo University– Egypt and the National Research Centre (NRC). This work was supported by Cairo
University.The authors sincerely extend their gratitude to Dr. Soha Mohamed Abd Elwahab for her unwavering support.

Declaration of competing interest

The authors declare that they have no known competing financial interests or personal relationships that could have appeared to influence the work accounted in this article.

Data Availability

Data will be made available on request.

Reference

[1] Hashim, Ahmed, and Zinah Hamad. "Lower cost and higher UV-absorption of polyvinyl alcohol/silica nanocomposites for potential applications." Egyptian Journal of Chemistry 63.2 (2020): 461-470.
[2] Gaaz, Tayser Sumer, et al. "Properties and applications of polyvinyl alcohol, halloysite nanotubes and their nanocomposites." Molecules 20.12 (2015): 22833-22847.
[3] Abdullah, Zainab Waheed, et al. "PVA, PVA blends, and their nanocomposites for biodegradable packaging application." Polymer-Plastics Technology and Engineering 56.12 (2017): 1307-1344.
[4] El-Shahat, Samar, et al. "Reduced Graphene Oxide/Zinc Oxide/Silver Nanocomposites Trigger Visible Light Activity for Efficient Photocatalytic Degradation of Xylenol Orange as a Persistent Pollutant Model." Egyptian Journal of Chemistry (2025).
[5] Feldman, Dorel. "Poly (vinyl alcohol) nanocomposites: Recent contributions to engineering and medicine." AIMS Mater. Sci 8.1 (2021): 119-129.
[6] Ramanathan, Ramarajan, et al. "Zinc stannate (Zn2SnO4)-based hybrid composite photoanode for dye-sensitized solar cell application." ACS Applied Energy Materials 5.9 (2022): 11506-11516.
[7] Abd El-Ghany, W. A., et al. "Optimization of the structural, optical and electrical properties of PVA/V2O5 for shielding applications." Radiation Physics and Chemistry 219 (2024): 111656.
[8] Huang, Xingyi, and Pingkai Jiang. "Core–shell structured high-k polymer nanocomposites for energy storage and dielectric applications." Advanced Materials 27.3 (2015): 546-554.
[9] Gupta, Rakesh K., Elliot Kennel, and Kwang-Jea Kim, eds. Polymer nanocomposites handbook. CRC press, 2009.
[10] Kharat, Prashant B., et al. "Induction heating analysis of surface-functionalized nanoscale CoFe2O4 for magnetic fluid hyperthermia toward noninvasive cancer treatment." ACS omega 5.36 (2020): 23378-23384.
[11] Nalbandian, Lori, et al. "Magnetic nanoparticles in medical diagnostic applications: synthesis, characterization and proteins conjugation." Current Nanoscience 12.4 (2016): 455-468.
[12] Li, Xin, et al. "Enhanced gas sensing properties for formaldehyde based on ZnO/Zn2SnO4 composites from one-step hydrothermal synthesis." Journal of Alloys and Compounds 850 (2021): 156606.
[13] Huang, Ruru, et al. "Crystallization behavior of polyvinyl alcohol with inorganic nucleating agent talc and regulation mechanism analysis." Journal of Polymers and the Environment 30.8 (2022): 3163-3173.
[14] Alhusaiki-Alghamdi, H. M. "Nanocomposite films of Zinc Oxide (ZnO) Nanorods/Polyacrylamide (PAM)/Polyvinyl alcohol (PVA) for Electronic devices Applications." Journal of Nanoelectronics and Optoelectronics 18.10 (2023): 1131-1139.
[15] Nowick, A. S. "X-ray diffraction procedures for polycrystalline and amorphous materials. HP Klug and LE Alexander. John Wiley and Sons, Inc., New York (1954). 716 pages. $15.00." AIChE Journal 2.1 (1956): 140-140.
[16] Patterson, A. L. "The Scherrer formula for X-ray particle size determination." Physical review 56.10 (1939): 978.
[17] El Desouky, Fawzy G., M. M. Saadeldin, and I. K. El Zawawi. "Synthesis and tuning the structure, morphological, optical, and photoluminescence properties of heterostructure cerium oxide and tin oxide nanocomposites." Journal of Luminescence 241 (2022): 118450.
[18] Abhijith, A. R., A. K. Srivastava, and Amar Srivastava. "Synthesis and characterization of magnesium doped ZnO using chemical route." Journal of Physics: Conference Series. Vol. 1531. No. 1. IOP Publishing, 2020.
[19] Mihaiu, Susana, et al. "Advanced ceramics in the SnO2–ZnO binary system." Ceramics International 41.3 (2015): 4936-4945.
[20] Gong, Xinghou, et al. "Characterization of poly (vinyl alcohol)(PVA)/ZnO nanocomposites prepared by a one-pot method." Composites Part B: Engineering 60 (2014): 144-149.
[21] Chandrakala, H. N., et al. "The influence of zinc oxide–cerium oxide nanoparticles on the structural characteristics and electrical properties of polyvinyl alcohol films." Journal of Materials Science 47 (2012): 8076-8084.
[22] Sabr, Ohood Hmaizah, et al. "Study the effect of zinc oxide nanoparticles on degradation, antibacterial, thermal and morphological properties of polyvinyl alcohol films." Journal of PRODUCTION ENGINEERING ARCHIVES 30(4) (2024): 528-536.
[23] Lee, Jihye, Kyung Jin Lee, and Jyongsik Jang. "Effect of silica nanofillers on isothermal crystallization of poly (vinyl alcohol): In-situ ATR-FTIR study." Polymer testing 27.3 (2008): 360-367.
[24] Ahmed, Eman H., and Magdy Mohamed Ayoub. "Investigation and Characterization of Physical Properties and Phonon modes of ZnO/PVA/PANI for Photonic Crystals application." Egyptian Journal of Chemistry 67.10 (2024): 383-388.
[25] Tjong, Sie Chin. "Structural and mechanical properties of polymer nanocomposites." Materials Science and Engineering: R: Reports 53.3-4 (2006): 73-197.
[26] Rashmi, S. H., et al. "Influence of zinc oxide nanoparticles on structural and electrical properties of polyvinyl alcohol films." Plastics, Rubber and Composites 44.1 (2015): 33-39.
[27] Gong, Xinghou, et al. "Characterization of poly (vinyl alcohol) (PVA)/ZnO nanocomposites prepared by a one-pot method." Composites Part B: Engineering 60 (2014): 144-149.

[28] Sikder, Mithun, et al. "Nanoparticle size and natural organic matter composition determine aggregation behavior of polyvinylpyrrolidone coated platinum nanoparticles." Environmental Science: Nano 7.11 (2020): 3318-3332.
[29] Gadelmawla, Elamir S., et al. "Roughness parameters." Journal of materials processing Technology 123.1 (2002): 133-145.
[30] Bhushan, Bharat. Modern tribology handbook, two volume set. CRC press, 2000.
[31] Kumar, B. Rajesh, and T. Subba Rao. "AFM studies on surface morphology, topography and texture of nanostructured zinc aluminum oxide thin films." Digest Journal of Nanomaterials and Biostructures 7.4 (2012): 1881-1889.
[32] Kumar, ABV Kiran, et al. "Silver nanowire/polyaniline composite transparent electrode with improved surface properties." Materials Research Bulletin 57 (2014): 52-57.
[33] Alpuche-Aviles, Mario A., and Yiying Wu. "Photoelectrochemical study of the band structure of Zn_2SnO_4 prepared by the hydrothermal method." Journal of the American Chemical Society 131.9 (2009): 3216-3224.
[34] Dai, Yibo, et al. "Enhanced mechanical, thermal, and UV-shielding properties of poly (vinyl alcohol)/metal–organic framework nanocomposites." RSC advances 8.67 (2018): 38681-38688.
[35] Mora, Enrique Sánchez, et al. "Morphological, optical and photocatalytic properties of TiO2–Fe_2O_3 multilayers." Solar energy materials and solar cells 91.15-16 (2007): 1412-1415.
[36] Memming, Rüdiger. Semiconductor electrochemistry. John Wiley & Sons, 2015.
[37] Tauc, Jan, ed. Amorphous and liquid semiconductors. Springer Science & Business Media, 2012.
[38] Cesarini, Gianmario, et al. "Quantitative evaluation of emission properties and thermal hysteresis in the mid-infrared for a single thin film of vanadium dioxide on a silicon substrate." International Journal of Thermal Sciences 146 (2019): 106061.
[39] Kumi-Barimah, E., et al. "Phase evolution, morphological, optical and electrical properties of femtosecond pulsed laser deposited TiO2 thin films." Scientific Reports 10.1 (2020): 10144.
[40] Sagadevan, Suresh, et al. "Hydrothermal synthesis of zinc stannate nanoparticles spectroscopic investigation." Journal of Materials Science: Materials in Electronics 28 (2017): 11268-11274.
[41] Aslam, Muhammad, Mazhar Ali Kalyar, and Zulfiqar Ali Raza. "Fabrication of nano-CuO-loaded PVA composite films with enhanced optomechanical properties." Polymer Bulletin 78 (2021): 1551-1571.
[42] Rajesh, K., et al. "Effect of ZnO nanofiller on dielectric and mechanical properties of PVA/PVP blend." AIP Conference Proceedings. Vol. 2162. No. 1. AIP Publishing, 2019.
[43] Ravati, Sepehr, and Basil D. Favis. "Low percolation threshold conductive device derived from a five-component polymer blend." Polymer 51.16 (2010): 3669-3684.
[44] Al-Saleh, Mohammed H., and Uttandaraman Sundararaj. "An innovative method to reduce percolation threshold of carbon black filled immiscible polymer blends." Composites Part A: Applied Science and Manufacturing 39.2 (2008): 284-293.
[45] Mao, Cui, Yutian Zhu, and Wei Jiang. "Design of electrical conductive composites: tuning the morphology to improve the electrical properties of graphene filled immiscible polymer blends." ACS applied materials & interfaces 4.10 (2012): 5281-5286.
[46] Min, Chao, et al. "A graphite nanoplatelet/epoxy composite with high dielectric constant and high thermal conductivity." Carbon 55 (2013): 116-125.
[47] Volkov, Aleksandr Sergeevich, et al. "Analysis of experimental results by the Havriliak–Negami model in dielectric spectroscopy." Optics and Spectroscopy 124 (2018): 202-205.
[48] Ommeish, Qamar, et al. "Synthesis and dielectric characterization of a bagasse cellulose/magnetite nanocomposite." Indian Journal of Physics (2024): 1-20.
[49] Kumar, NB Rithin, Vincent Crasta, and B. M. Praveen. "Dielectric and electric conductivity studies of PVA (Mowiol 10-98) doped with MWCNTs and WO3 nanocomposites films." Materials Research Express 3.5 (2016): 055012.
[50] Shen, Zhong-Hui, et al. "Space charge effects on the dielectric response of polymer nanocomposites." Applied Physics Letters 111.9 (2017).
[51] Ghasemi, Ali, et al. "Enhanced reflection loss characteristics of substituted barium ferrite/functionalized multi-walled carbon nanotube nanocomposites." Journal of Applied Physics 109.7 (2011).
[52] Mohamed Ali, T., N. Padmanathan, and S. Selladurai. "Structural, conductivity, and dielectric characterization of PEO–PEG blend composite polymer electrolyte dispersed with TiO 2 nanoparticles." Ionics 19 (2013): 1115-1123.
[53] Salam, Omar Abdel, et al. "A comparative study of PMMA/PEG polymer nanocomposites doped with different oxides nanoparticles for potential optoelectronic applications." Scientific Reports 14.1 (2024): 19295.
[54] Latif, I., et al. "Preparation, characterization and electrical study of (carboxymethylated polyvinyl alcohol/ZnO) nanocomposites." American Journal of Polymer Science 2.6 (2012): 135-140.
[55] Şenarslan, Elvan, and Mustafa Sağlam. "Voltage-frequency dependence of the complex dielectric and electric modulus and the determination of the interface-state density distribution from the capacitance-frequency measurements of Al/p-Si/Al and Al/V2O5/p-Si/Al structures." Applied Physics A 130.9 (2024): 641.
[56] Efil, E., et al. "Frequency dependent dielectric properties of atomic layer deposition grown zinc-oxide based MIS structure." Physica B: Condensed Matter 568 (2019): 31-35.
[57] Roumaih, Kh. "Effect of temperature on the dielectric and magnetic properties of NiFe2O4@ $MgFe_2O_4$ and $ZnFe_2O_4$@ $MgFe_2O_4$ core-shell." Physica Scripta 96.12 (2021): 125809.
[58] Dridi, R., et al. "Structural, optical and AC conductivity studies on alloy ZnO–Zn_2SnO_4 (ZnO–ZTO) thin films." Journal of Alloys and Compounds 634 (2015): 179-186.